PCCP

Accepted Manuscript

ROYAL SOCIETY OF CHEMISTRY

www.rsc.org/pccp

Using lithium carbonate-based electron injection structures in high-performance inverted organic light-emitting diodes

Chih-Hao Chang,[1,]* Ming-Kuan Hsu,[1] Szu-Wei Wu,[1] Mei-Hsin Chen,[2,]* Hung-Hsuan Lin,[2]
Chia-Shou Li[3], Tun-Wen Pi,[4] Hsin-Hua Chang,[5,]* Nien-Po Chen[1]

[1]*Department of Photonics Engineering, Yuan Ze University, Chung-Li, Taiwan 32003*

[2]*Department of Opto-Electronic Engineering, National Dong Hwa University, Hualien 974, Taiwan*

[3]*Graduate Institute of Photonics and Optoelectronics, National Taiwan University, Taipei 106, Taiwan*

[4]*National Synchrotron Radiation Research Center, Hsinchu, Taiwan 300, Taiwan*

[5]*Department of Electro-Optical Engineering, Vanung University, Chung-Li, Taiwan 32061*

E-mail: chc@saturn.yzu.edu.tw; Fax: + 886 3 4638800 ext. 7517; Tel: + 886 3 4514281

E-mail: meihsinchen@mail.ndhu.edu.tw; Fax: + 886 3 8634180; Tel: + 886 3 634192

E-mail: hhua3@mail.vnu.edu.tw; Fax: +886 3 4515811 ext. 73001; Tel: +886 3 4515811 ext. 73607

Abstract

A lithium carbonate-based bi-layered electron injection layer was introduced into inverted organic light-emitting diodes (OLEDs) to reduce operation voltages and achieve carrier balance. Ultraviolet photoemission spectroscopy was used to confirm the existence of an interfacial dipole between the organic and lithium carbonate layers, which is a dominating factor related to the device performance. Respective maximum efficiencies of 15.9%, 16.9%, and 8.4% were achieved for blue, green, and red phosphorescent inverted OLEDs with identical architectures, indicating that carrier balance was easily obtained. Moreover, adopting this sophisticated electron injection layer design resulted in respective turn on voltages of only 3.4 V, 3.2 V, and 3.2 V. Furthermore, the inverted OLEDs equipped with silicon dioxide nanoparticles based light-extraction films achieved an approximately 1.3-fold efficiency improvement over pristine devices due to the low refractive index of the silicon dioxide nanoparticles along with the effective scattering function. The blue, green, and red inverted OLEDs with the nanocomposite layer achieved respective peak efficiencies of 20.9%, 21.3%, and 10.1%.

Keywords: Lithium carbonate, electron injection material, inverted organic light-emitting diodes, silicon dioxide, light-extraction.

Introduction

Phosphorescence can use both singlet and triplet exciton, thus in principle internal quantum efficiencies of nearly 100% could be achieved, as opposed to the 25% upper limit imposed by the formation of singlet excitons in fluorescence. Thus, phosphorescent OLEDs have received considerable attention in recent years because of their excellent performance in both display and lighting applications. At the same time, bottom-emission inverted organic light-emitting diodes (IOLEDs) have drawn attention because of their easy integration with transparent metal oxide based thin film transistors (TFT). In addition, OLEDs with inverted architectures provide longer device lifetimes because such structures keep water- and oxygen-sensitive electron injection materials beneath the organic and metal layers.[1-2] However, bottom-emission inverted OLEDs still face some problems such as high operation voltages and low efficiency levels. Therefore, there is high demand to raise IOLED performance levels to those comparable to conventionally-structured devices.

In contrast to conventional OLEDs, in inverted OLEDs the device architecture adopts a bottom cathode and a top anode. Therefore, the corresponding organic layers should be rearranged opposite to the original stacking. If a metal layer is used as the cathode to decrease the energy barrier and provide sufficient electron injection, the bottom metal cathode combined with top metal anode will form a strong microcavity effect. Spectral variations in different viewing angles resulting from the microcavity effect make this approach unsuitable for use in display applications. Thus, to avoid the microcavity effect, ITO and metal must respectively be used as a transparent cathode and reflective anode. However, the high energy barrier formed at the interface between the ITO and organic layer restricts the electron injection to the lowest unoccupied molecular orbital (LUMO), resulting in a higher operation voltages and carrier imbalance. In general, the high work function (WF) of ITO (i.e. 4.7 eV) could be modified by evaporating electron injection materials, which could induce a strong dipole. The interfacial dipole provides the interface with states to attract carriers. On the other hand, n-type doping methods are also useful for the energy band bending of organic layers, thus enhancing the electron injection current. Previous studies have shown success using some n-type dopants like Cs, Li, MgO, CsOH, Cs_2O, Cs_2CO_3, Rb_2CO_3, Li_2CO_3 etc.[3-11] For instance, in 2012 Lee's group reported a novel effective electron injection layer (EIL) consisting of TmPyPB doped with Yb.[10] The external quantum efficiency and luminance efficiency of this FIrpic-based IOLED were 8.6% and 15.3 cd/A, respectively, with a turn-on voltage of about 4.5 V. The same year, Ma reported using a PEI:Li_2CO_3 layer as an EIL in blue, green, and red phosphorescent IOLEDs to achieve respective external quantum efficiencies of 15.2%, 16.2%, and 10.8%.[11] In addition, the respective operation voltages of the blue, green, and red IOLEDs were recorded as 4.3V, 3.9 V, and 4.5 V. Overall, more attention has been focused on metal carbonates due to the relatively high degree of control achieved during evaporation as compared to highly active metals. However, previous studies reported that the turn-on voltages of FIrpic-based IOLEDs fall within a range from 4 to 8 V,[10-13] higher than that of conventional bottom-emission OLEDs. In addition, some metal carbonates that are high levels of deliquescence might reduce device lifetime. However, few studies have sought to determine appropriate electron injection materials which are stable in atmospheric environments and produce no deliquescence.

In this study, we compared two commonly-used metal carbonates as the electron injection materials in an atmospheric environment and combined interfacial dipoles with the n-type doping method to boost the current density of IOLEDs. The effective EIL consisted of a non-doped metal carbonate layer and a metal carbonate doped organic layer. This EIL design was used as the basis for developing blue, green and red phosphorescent IOLEDs, achieving respective turn-on voltages of 3.4 V, 3.2 V, and 3.2 V for the blue, green, and red devices. By using an identical architecture in IOLEDs with different emissive dopants, we found that this architecture easily achieved carrier balance and had high potential for mass production.

Moreover, an external light-extraction structure was used to further improve the IOLED performance. The blue, green, and red phosphorescents with light extraction structures achieved respective peak efficiencies of 18.5%, 22.3%, and 9.7%.

Experimental

Ultraviolet photoemission spectroscopy (UPS) measurements. To obtain superior resolution, UPS was performed at the National Synchrotron Radiation Research Center (NSRRC), Hsinchu, Taiwan, R.O.C. A high-brightness photon beam was generated using a bending magnet active grating monochromator. Photoemission experiments were conducted in an ultra-high vacuum chamber, and the UPS was obtained *in situ* immediately after each deposition. The UPS spectrum was measured using with photon energy of 40.8 eV under a base pressure of 7.5×10^{-13} Pa. Changes in the energy position of the highest occupied molecular orbital (HOMO) caused by the deposition of Li_2CO_3 can be observed by aligning the Fermi level obtained from measurements of clean gold films. Changes in the vacuum level were identified using a sample bias of -8 V to observe the onset at lower binding energies in the UPS spectra.

Nanocomposite scattering film. According to the waveguide optics, the radiation mode of OLEDs is only about 20% to 25%, which could be improved by adopting light-extraction structures. External light-extraction structures are easily assembled, and do not affect the electrical properties of the device. Silicon dioxide (SiO_2) nanoparticles (NPs) can be used in external extraction structure (EES) because they can be produced in various sizes and have a refractive index close to that of air. In addition, we selected a transparent polydimethylsiloxane (PDMS) as the host material for SiO_2 NPs. The nanocomposite films were assembled in three simple steps, discussed in our previous work.[12] Herein, two kinds of substrates were used to test IOLED performance, namely Substrate I and Substrate II. Substrate I is a commercially-available ITO-coated glass substrate used to fabricate the control device. The SiO_2 nanocomposite film-coated on ITO-coated glass (i.e. Substrate I) is named Substrate II and is used as an experimental counterpart. In general, the Haze of the scattering films could be increased by adopting NPs of a size similar to the wavelength of incident light. Nevertheless, mixing NPs of such sizes in the solution usually results in severe aggregation and concomitantly reduces the scattering capability. Furthermore, the smaller NPs could serve as an effective dispersant in the nanocomposite films.[14] As such, 250 nm SiO_2 NPs were selected to scatter objects in Substrate II. In addition, the 25 nm NPs could fill up the pores and then stretch the distance between the 250 nm-NPs, thus drastically flattening the coarse surface and boosting the scattering capability. Hence, both 25 nm- and 250 nm-SiO_2 were uniformly mixed in the transparent PDMS to produce an effective scattering film.

OLED Fabrication. ITO film was selected as the transparent anode material for OLED fabrication. The organic materials including iridium complexes were purchased from Nichem and Lumtec. All organic compounds were subjected to temperature-gradient sublimation under high vacuum before use. The organic and metal layers were deposited by vacuum evaporation in a vacuum chamber with a base pressure of $<10^{-6}$ Torr. The deposition system enabled the fabrication of the complete device structure without breaking the vacuum. The active area of the device was set to 2×2 mm^2, as defined by the shadow mask used for cathode deposition. Current density-voltage-luminance characterization was measured using a Keithley 238 current source-measure unit and a Keithley 6485 picoammeter equipped with a calibrated Si-photodiode. The electroluminescent spectra of the devices were recorded using an Ocean Optics spectrometer. The bright-field microscope images were taken by an optical microscope (PoTop, HVC-300-CA).

Results and Discussion

(i) Stability test of cesium carbonate and lithium carbonate

For the carrier to overcome the energy barriers between the electrodes and the organic layers requires using an appropriate material that forms strong dipoles to boost the carrier injection. Consequently, we used two commonly-used inorganic salt electron injection materials, cesium carbonate (Cs_2CO_3) and lithium carbonate (Li_2CO_3) . Since 2004, Cs_2CO_3 had been intensively used as n-type dopant in electron transport materials or as electron injection materials in OLEDs or solar cells. Extensive studies have found that the electron injection mechanism of Cs_2CO_3 is the formation of an Al–O–Cs structure at the interface between Cs_2CO_3 and Al,[8] which evidently enhances the electron injection. Furthermore, in addition to changing the Fermi level of the organic electron transport materials, Cs_2CO_3 can also be used to modify the work function of the electrodes because of the formation of surface dipoles. On the other hand, Li_2CO_3 has also been shown to be an effective n-type dopant or electron injection material. Nevertheless, Li_2CO_3 is less well-understood because of the widespread success of Cs_2CO_3 as effective n-type dopant. In addition, few reports have discussed the stability of both alkali metal carbonates, although the stability of EIL has a critical influence on device lifespan. Consequently, both Cs_2CO_3 and Li_2CO_3 were used to examine device stability in an atmospheric environment. The structure consisted of ITO/ Cs_2CO_3 or Li_2CO_3 (50 nm)/ Al (150 nm). Figure 1 shows the bright-field microscopy images of the samples at different times after removal from the chamber. Small bubbles are seen to appear on top of the Cs_2CO_3 sample from the beginning. After three minutes, black spots begin to appear in increasing numbers. In contrast, the Li_2CO_3 sample exhibits great stability in the atmospheric environment. In addition, the inherent deliquescence property abruptly boosts the pressure during the evaporation of Cs_2CO_3. Steam released in this process is probably harmful to device lifetime. Therefore, Li_2CO_3 was chosen as the electron injection material in the following experiments.

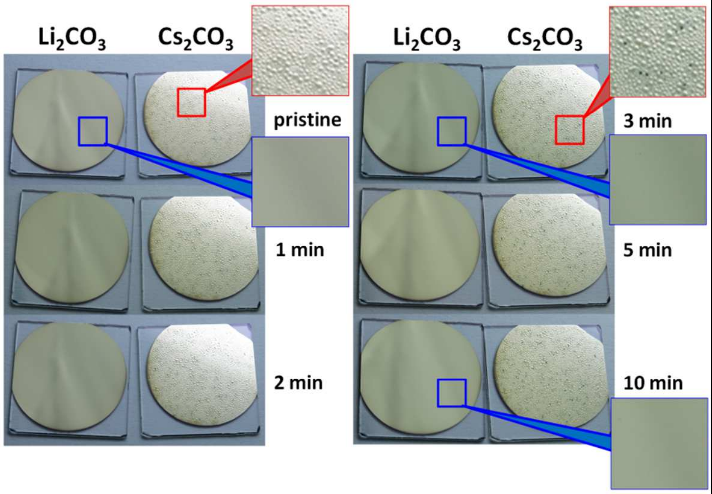

Fig. 1 The bright-field microscope images of Li_2CO_3 and Cs_2CO_3 samples at different times after removal from the chamber.

(ii) Sophisticated structure design of the electron injection layer

To investigate the electron injection capability of the selected materials, single carrier devices with different EIL structures were created as follows: (Device S1) ITO/ TmPyPB (75 nm)/ TAPC (10 nm)/ Al (150 nm); (Device S2) ITO/ Li_2CO_3 (5 nm)/ TmPyPB (70 nm)/ TAPC (10 nm)/ Al (150 nm); (Device S3) ITO/ TmPyPB doped with 20 wt.% of Li_2CO_3 (5 nm)/ TmPyPB (70 nm)/ TAPC (10 nm)/ Al (150 nm); (Device S4) ITO/ Li_2CO_3 (5 nm)/ TmPyPB doped with 20 wt.% of Li_2CO_3 (5 nm)/ TmPyPB (65 nm)/ TAPC (10 nm)/ Al (150 nm). 1,3,5-tri[(3-pyridyl)-phen-3-yl]benzene (TmPyPB) and di-[4-(N,N-ditolyl-amino)-phenyl] cyclohexane (TAPC) were respectively selected as the electron-transport layer and electron blocking layer due to their excellent carrier transport capabilities and adequate energy gaps.[15-16] A structure consisting of a single Li_2CO_3 layer was used to examine the effectiveness of the interfacial dipole; while a structure consisting of single TmPyPB doped with a Li_2CO_3 layer was used to test the capability of n-type doping.

Figure 2 shows the current density-voltage curves of the tested single carrier devices. The current density trend of each tested single carrier device was as follows: (S1) < (S2) < (S3) <

(S4). As expected, the carrier could not inject into the organic layers without EIL. In addition, the device with a single Li_2CO_3 layer could provide effective interfacial dipoles to facilitate electron injection from ITO to the organic layers. Furthermore, devices using Li_2CO_3 as an n-type dopant in TmPyPB layer (i.e. Device S3) exhibited even higher current density than those with a single Li_2CO_3 layer. This implies that TmPyPB could interact with the Li_2CO_3 resulting in a energy band bending. Thus, the energy barrier between ITO and the Li_2CO_3 doped layer was significantly mitigated. Overall, Device S4, consisting of both a non-doped Li_2CO_3 layer and a Li_2CO_3 doped layer, possessed a highest current density, indicating the effectiveness of EIL by combining both functions of Li_2CO_3. Ultraviolet photoelectron spectroscopy (UPS) was used to further confirm the mechanism of Li_2CO_3 enhancement in electron injection.

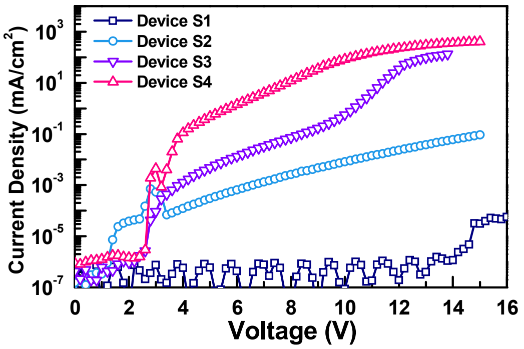

Fig. 2 The current density of the tested single carrier devices.

The UPS spectra near the onset and the HOMO were obtained to determine the correlation between device performance and changes to electronic states at the interfaces. Figure 3(a) shows the UPS spectra of the TmPyPB layer following the deposition of Li_2CO_3. The energy band diagrams shown in Figure 3(b) can be deduced from UPS spectra, and the HOMO level was defined by extrapolating the edges of the HOMO peak to the background of the UPS spectra. The band gap of the TmPyPB layer is 3.95 eV, which can be obtained from optical absorption data.[15,17] The HOMO level of the TmPyPB layer is 3.25 eV below the Fermi level

(E_F), which means that the LUMO level is only 0.70 eV above the E_F. This indicates that the pristine TmPyPB layer is a strong n-type material, thus the energy levels of the HOMO and LUMO do not shift obviously with the deposition of a few angstroms of Li_2CO_3. On the other hand, the onset position of the UPS spectrum shifts toward a higher binding energy by 0.3 eV following the deposition of Li_2CO_3, resulting from the existence of interfacial dipoles,[18] which can benefit the charge transport and lead to better efficiency. Therefore, the dominating factor which enhances device performance is the interfacial dipole at the interfaces between TmPyPB and Li_2CO_3. Thus, according to the experimental outcomes, the bi-layer structure with Li_2CO_3 was selected as the electron injection layer for the OLEDs.

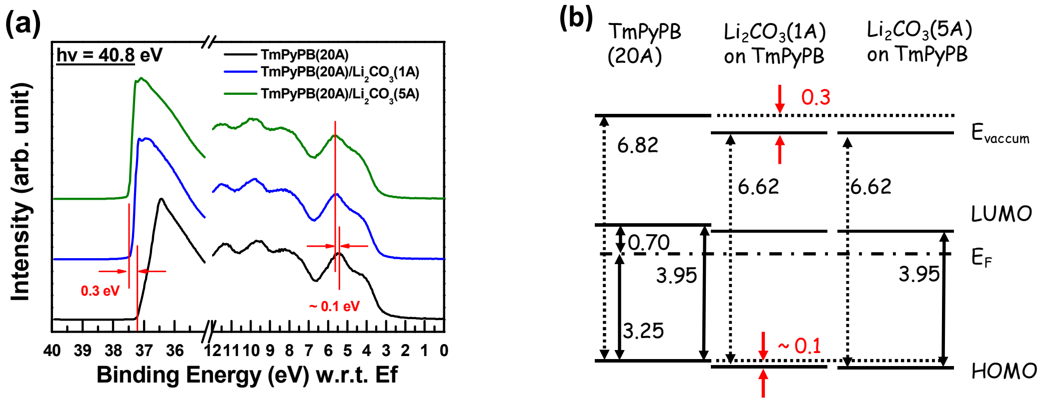

Fig. 3 (a) UPS spectra of the $TmPyPB/Li_2CO_3$ films; (b) energy band diagrams of the $TmPyPB/Li_2CO_3$ films.

(iii) Blue, green, and red phosphorescent IOLEDs using an identical device architecture

In this study, we attempted to develop blue, green and red phosphorescent IOLEDs based on a single architecture. It should be noted that the blue phosphor is the key to successful IOLED design, as it produces the shortest wavelength emissions. Thus such devices should use wide-gap host and wide-gap carrier transporting materials. Iridium(III) FIrpic, $Ir(ppy)_3$, and $Ir(piq)_3$ were respectively selected as the blue, green, and red phosphorescent emitters because of their high quantum yields. Furthermore, bipolar 3-bis(9-carbazolyl)benzene (mCP) with a wide-triplet energy gap of 2.9 eV was used to fulfill the requirements of endothermic energy transfer from the host to the blue, green, and red guests. The hole and electron mobilities of mCP are respectively measured at 1.2×10^{-4} and 3.4×10^{-5} cm^2/Vs.[19] Most importantly, devices using a bipolar host are better able to achieve carrier balance, especially in inverted architectures. The ideal hole injection materials could be selected by testing different materials to achieve optimal carrier balance. Two commonly used hole injection materials (HIM), HATCN and MoO_3, were used for comparison. From the EL characteristics, the blue inverted OLEDs with both HIMs show similar efficiency levels of about 16%, implying that this bi-layer EIL design easily achieved carrier balance. Because the device with HATCN exhibited slightly higher efficiency levels as well as mitigated efficiency roll-off, HATCN was chosen as the hole injection layer. Consequently, the optimized architecture for blue, green, and red IOLEDs was: Substrate I or Substrate II/ ITO (120 nm)/ Li_2CO_3 (5 nm)/ TmPyPB doped with 20 wt.% Li_2CO_3 (5 nm)/ TmPyPB (50 nm)/ mCP doped with 8 wt.% phosphorescent emitter (30 nm)/ TAPC (15 nm)/ HATCN (10 nm)/ Al (150 nm). FIrpic, $Ir(ppy)_3$ and $Ir(piq)_3$ were respectively used as the phosphorescent emitters for the blue, green, and red IOLEDs. Figure 4 shows a structural drawing of the materials, along with the schematic structures of the tested OLEDs.

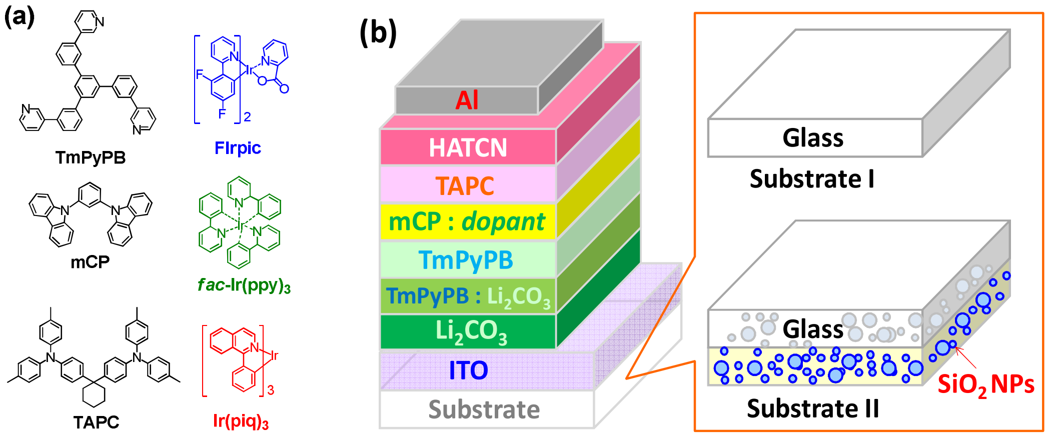

Fig. 4 (a) Chemical structures of the organic materials; (b) schematic architecture of the tested inverted OLEDs and substrates.

Figure 5 and Table 1 show the EL characteristics of phosphorescent IOLEDs with different substrates, including Devices I (Substrate I), and II (Substrate II). All tested devices display an EL spectrum with a notable vibronic structure similar to their photoluminescence. The lack of other emissions implies that the carrier recombination zone was located within the emitting layer and that the exciton diffusion to the adjacent carrier transport layers could be avoided. The small variations in the emission wavelength observed between devices with different substrates were presumably associated with the concurrent changes in the optical effects. Both Devices I and II exhibited stable emissions for brightness levels from 10^2 to 10^4 cd/m^2.

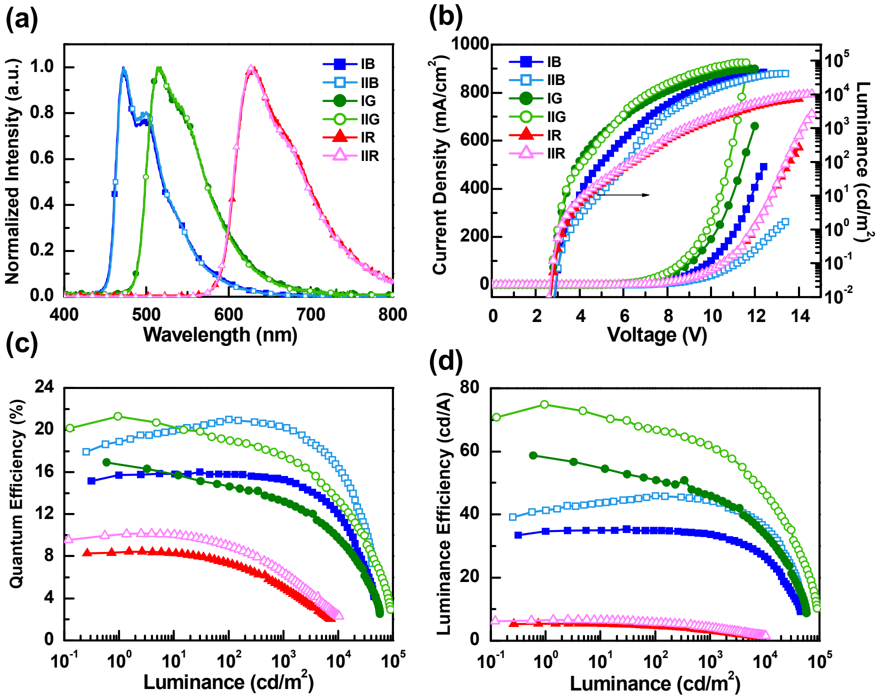

Fig. 5 (a) EL spectra of Devices IB, IIB, IG, IIG, IR, and IIR; (b) current density-voltage-luminance (*J*-*V*-*L*) curves; (c) external quantum efficiency vs. luminance; (d) luminance efficiency vs. luminance for devices IB, IIB, IG, IIG, IR, and IIR.

Table I. EL characteristics of tested IOLEDs with different substrates.

Device	IB	IIB	IG	IIG	IR	IIR
dopant	FIrpic		*fac*-Ir(ppy)$_3$		Ir(piq)$_3$	
Substrate	I	II	I	II	I	II

External Quantum Efficiency (%)	[a]	15.9	20.9	16.9	21.3	8.4	10.1
	[b]	15.7	20.9	14.6	19.0	7.2	8.9
Luminance Efficiency (cd/A)	[a]	35.2	45.8	58.7	74.8	5.3	6.5
	[b]	34.8	45.8	50.8	66.7	4.6	5.7
Power Efficiency (lm/W)	[a]	32.8	38.4	61.5	79.4	5.5	6.9
	[b]	21.1	23.2	39.9	49.9	2.4	2.8
Turn on Voltage (V)	[c]	3.4	3.5	3.2	3.2	3.2	3.2
Max. Luminance (cd/m^2) [V]		45073 [12.4 V]	41844 [13.4 V]	57671 [12.0 V]	90067 [11.6 V]	8983 [14.0 V]	10191 [14.6 V]
CIE 1931 Coordinates	[b]	(0.17,0.37)	(0.17,0.37)	(0.33,0.61)	(0.35,0.61)	(0.68,0.32)	(0.68,0.32)
	[d]	(0.17,0.37)	(0.17,0.38)	(0.33,0.61)	(0.34,0.61)	(0.68,0.32)	(0.68,0.32)

[a] Maximum efficiency; [b] recorded at 10^2 cd/m^2; [c] turn-on voltage measured at 1 cd/m^2; [d] measured at 10^3 cd/m^2.

The turn-on voltage of Device IB using FIrpic as emitter was measured at 3.4 V, which is lower than in most previous reports. In terms of the efficiency of the applied forward bias, Device IB exhibited a peak external quantum efficiency of 15.9 %, a luminance efficiency (LE) of 35.2 cd/A, and a power efficiency (PE) of 32.8 lm/W. Moreover, at a practical luminescence of 10^2 cd/m^2 the efficiencies were sustained at high values, with efficiencies of 15.7 %, 34.8 cd/A, and 21.1 lm/W. The satisfactory efficiencies and low operation voltages showed that this sophisticated EIL provides superior electron injection performance and allows for carrier balance adjustments in the device. Furthermore, the bipolar capability of mCP could enable the exciton formation zone to spread through the entire emitting layer (EML), thus reducing the concentration of the triplet exciton in a narrow space and easing triplet-triplet annihilation.[20] Similarly, both Devices IG and IR (which have the same architecture) also exhibited high efficiencies and low operation voltages, indicating that the sophisticated designs incorporating electron injection layers and bipolar host materials simultaneously achieves carrier balance in blue, green and red IOLEDs. The same turn-on voltage of 3.2 V was obtained in Devices IG and IR. Device IG exhibited high efficiencies of 14.6 %, 50.8 cd/A, and 49.9 lm/W at a practical brightness of 10^2 cd/m^2; while Device IR exhibited efficiencies of 7.6%, 4.6 cd/A and 2.4 lm/W. More exactly, the peak efficiencies of Devices IG and IR respectively reached 16.9% (58.7 cd/A, 61.5 lm/W) and 8.4% (5.3 cd/A, 5.5 lm/W). In comparison to the efficiency of the roll-off behaviors of the tested IOLEDs, the EQEs declined to one half at a current density ($J_{1/2}$) of 164.1, 55.1 and 66.3 mA/cm^2, respectively, for Devices IB, IG and IR. The significantly mitigated efficiency roll-off observed in Device IB might be due to the adequate energy relationship between the host and guest. Moreover, the carrier trapping resulting from dopants with lower energy gaps might also influence the exciton concentration in the EML. Although the $J_{1/2}$ values of Device IB were higher, the $J_{1/2}$ values of both Devices IG and IR were satisfactory compared to those of other phosphorescent OLEDs.

On the other hand, applying substrates with external nanocomposite films in IOLEDs enhanced the outcoupling efficiencies due to the scattering phenomenon. At a practical luminescence of 10^2 cd/m^2, Device IIB achieving an efficiency of 20.9% (45.8 cd/A and 38.4 lm/W), which is around 1.3 times the corresponding value for Device IB. The efficiency improvement was due to the low refractive index of the SiO_2 nanoparticles along with the effective scattering function. By combining SiO_2 nanoparticles of different sizes, we fabricated a nanocomposite substrate which simultaneously achieved a satisfactory film morphology, a low refractive index, and great scattering capability. Similar results were obtained in both green and red IOLEDs based on substrates with external light-extraction structures. The respective efficiencies of Devices IIG and IIR were up to 21.3% (74.8 cd/A, 79.4 lm/W) and 10.1% (6.5 cd/A, 6.9 lm/W). The turn on voltages of Devices IIG and IIR were identical at 3.2 V. These outcomes demonstrate that the combination of adequate EIL with an external light-extraction structure enables IOLEDs to meet the stringent requirements of n-channel TFTs.

In conclusion, a bi-layered EIL consisting of a Li_2CO_3 layer and a TmPyPB layer doped with Li_2CO_3 was used to mitigate the operation voltage in IOLEDs. Blue, green and red phosphorescent IOLEDs exhibited satisfactory respective efficiencies of 15.9%, 16.9%, and

8.4%. Furthermore, the respective turn on voltages of blue, green and red IOLEDs were only 3.4 V, 3.2 V and 3.2 V. This universal device architecture with tailor-made EIL provides superior electron injection performance and carrier balance in IOLEDs. To further improve performance, the IOLEDs were equipped with a SiO_2-based nanocomposite layer as the external light-extraction structure. These IOLEDs with a nanocomposite layer provided an approximately 1.3-fold efficiency improvement over pristine devices due to the low refractive index of the SiO_2 nanoparticles along with the effective scattering function.

The authors gratefully acknowledge the financial support from Ministry of Science and Technology of Taiwan (NSC 102-2221-E-155-080-MY3 and NSC 103-2623-E-155-008-ET).

Reference

1 P.-S. Wang, I.-W. Wu and C.-I. Wu, *J. Appl. Phys.*, 2010, **108**, 103714.

2 C. W. Chen, C. L. Lin and C. C. Wu, *Appl. Phys. Lett.*, 2004, **85**, 2469.

3 T. Dobbertin, O. Werner, J. Meyer, A. Kammoun, D. Schneider, T. Riedl, E. Becker, H.-H. Johannes and W. Kowalsky, *Appl. Phys. Lett.*, 2003, **83**, 5071.

4 H. W. Choi, S. Y. Kim, W.-K. Kim and J.-L. Lee, *Appl. Phys. Lett.*, 2005, **87**, 082102.

5 T.-Y. Chu, J.-F. Chen, S.-Y. Chen, C.-J. Chen and C. H. Chen, *Appl. Phys. Lett.*, 2006, **89**, 053503.

6 T. Xiong, F. Wang, X. Qiao and D. Ma, *Appl. Phys. Lett.*, 2008, **92**, 263305.

7 M. Thomschke, S. Hofmann, S. Olthof, M. Anderson, H. Kleemann, M. Schober, B. Lüssem and K. Leo, *Appl. Phys. Lett.*, 2011, **98**, 083304.

8 C. Yun, H. Cho, T.-W. Koh, J.-H. Kim, J. W. Kim, Y. Park and S. Yoo, *IEEE Trans. Electron Devices*, 2012, **59**, 159.

9 J.-H. Lee, P.-S. Wang, H.-D. Park, C.-I Wu and J.-J. Kim, *Org. Electron.*, 2011, **12**, 1763.

10 H. Lee, H. Ahn and C. Lee, *J. Korean Phys. Soc.*, **61**, 536-1540 (2012).

11 J. Chen, C. Shi, Q. Fu, F. Zhao, Y. Hu, Y. Feng and D. Ma, *J. Mater. Chem.*, 2012, **22**, 5164.

12 H. Lee, I. Park, J. Kwak, D. Y. Yoon and C. Lee, *Appl. Phys. Lett.*, 2010, **96**, 153306.

13 E. Najafabadi, K. A. Knauer, W. Haske, C. Fuentes-Hernandez and B. Kippelen, *Appl. Phys. Lett.*, 2012, **101**, 023304.

14 C.-H. Chang, K.-Y. Chang, Y.-J. Lo, S.-J. Chang and H.-H. Chang, *Org. Electron.*, 2012, **13**, 1073.

15 S.-J. Su, T. Chiba, T. Takeda and J. Kido, *Adv. Mater.*, 2008, **20**, 2125.

16 N. Chopra, J. Lee, Y. Zheng, S.-H. Eom, J. Xue and F. So, *Appl. Phys. Lett.*, 2008, **93**, 143307.

17 L. S. Cui, Y. L. Liu, Q. Li, Z. Q. Jiang and L. S. Liao, *Org. Electron.*, 2014, **15**, 1368.

18 H. Antoniadis, B. R. Hsieh, M. A. Abkowitz, S. A. Jenekhe and M.Stolka, *Synth. Met.* 1994, **62**, 265.

19 T. Tsuboi, S.-W. Liu, M.-F. Wu and C.-T. Chen, *Org. Electron.*, 2009, **10**, 1372.

20 M. A. Baldo, D. F. O'Brien, Y. You, A. Shoustikov, S. Sibley, M. E. Thompson and S. R. Forrest, *Nature*, 1998, **395**, 151.